J|A|C|S
ARTICLES
Published on Web 04/27/2006

Ultralow-Density Nanostructured Metal Foams: Combustion Synthesis, Morphology, and Composition

B. C. Tappan,* M. H. Huynh, M. A. Hiskey, D. E. Chavez, E. P. Luther, J. T. Mang, and S. F. Son

Contribution from the Los Alamos National Laboratory, Los Alamos, New Mexico 87545

Received September 23, 2005; E-mail: btappan@lanl.gov

Abstract: The synthesis of low-density, nanoporous materials has been an active area of study in chemistry and materials science dating back to the initial synthesis of aerogels. These materials, however, are most often limited to metal oxides, e.g., silica and alumina, and organic aerogels, e.g., resorcinol/formaldehyde, or carbon aerogels, produced from the pyrolysis of organic aerogels. The ability to form monolithic metallic nanocellular porous materials is difficult and sometimes elusive using conventional methodology. Here we report a relatively simple method to access unprecedented ultralow-density, nanostructured, monolithic, transition-metal foams, utilizing self-propagating combustion synthesis of novel transition-metal complexes containing high nitrogen energetic ligands. During the investigation of the decomposition behavior of the high-nitrogen transition metal complexes, it was discovered that nanostructured metal monolithic foams were formed in a post flame-front dynamic assembly having remarkably low densities down to 0.011 g cm^{-3} and extremely high surface areas as high as 270 m^2 g^{-1}. We have produced monolithic nanoporous metal foams via this method of iron, cobalt, copper, and silver metals. We expect to be able to apply this to many other metals and to be able to tailor the resulting structure significantly.

Introduction

Metal foams are a relatively new class of materials with unique combinations of properties such as high stiffness, low density, gas permeability, and thermal conductivity. As such, these materials promise to enable new technologies in areas as diverse as catalysis, fuel cells, hydrogen storage, and thermal and acoustical insulation. Techniques for making metal foams to date have been somewhat limited in scope (some exceptions are mentioned below) yielding relatively coarse structures (large pores) with relatively low surface area and high density compared to foam monoliths of other materials such as aerogel. Furthermore, approaches have concentrated on aluminum- or nickel-based materials although techniques for magnesium, lead, zinc, copper, titanium, steel, gold, and others have been studied.[1]

Conventional approaches to the synthesis of high surface area materials result in aerogels[2,3] with surface areas of 100 to 1000 m^2 g^{-1}, with the highest surface areas arising from carbon aerogels. Although these approaches have been extended to produce foams containing metal oxides such as a high surface area titania aerogel[4] with a Brunauer−Emmett−Teller (BET) measured surface of 100−200 m^2 g^{-1}, metallic foams of transition metals cannot be produced in this manner. Conventional approaches to make metallic foams follow fundamentally different paths and yield considerably lower surface area materials, generally with large pores. The lowest-density metal foams found in the literature range from 0.04 to 0.08 g cm^{-3} and are often made from magnesium or aluminum. As a penalty for the low density, however, these foams contain cells on the millimeter length-scale and, thus, have a relatively low surface area.[5,6] Recently, a silver sponge formed from the reduction of $AgNO_3$ on a dextran template was reported with pore sizes on the order of a few microns and a surface area of 0.5 m^2 g^{-1}; however, no density was reported.[7] Dendritic platinum three-dimensional foamlike nanostructures synthesized in an aqueous surfactant were also recently reported, but these are limited to very small clusters ranging in size from 6 to 200 nm.[8] Beiner et al. report a high-yield strength nanoporous gold structure produced via electrochemically driven de-alloying where Ag was electrolytically dissolved from a $Au_{0.42}Ag_{0.58}$ alloy using 75% nitric acid as the electrolyte. Their resulting Au, almost free of residual Ag, had a relative density of 42%, interconnecting ligaments on the order of 100 nm, a polycrystalline grain structure of approximately 10−60 nm, and surprisingly high yield strength.[9] Chemical vapor deposition (CVD) has also been applied to produce porous structures (10−1000 μm cell size) of refractory metals such as iridium and rhenium on carbon

(1) Ashby, M. F.; Evans, A.; Fleck, N. A.; Gibson, L. J.; Hutchinson, J. W.; Wasley, H. N. G.; *Metal Foams: A Design Guide*; Butterworth-Heinemann: Woburn, MA, 2000.
(2) Kistler, S. S. *Nature* **1931**, *127*, 741.
(3) Kistler, S. S. *J. Phys. Chem.* **1932**, *36*, 52.
(4) Suh, D. J.; Park, T. J. *Chem. Mater.* **1996**, *8*, 509.
(5) Gibson, L. *Annu. Rev. Mater. Sci.* **2000**, *30*, 191.
(6) Kanahashi, H.; Mukai, T.; Yamada, Y.; Shimojima, K.; Mabuchi, M.; Nieh, T. G.; Higashi, K. *Mater. Sci. Eng.* **2000**, *A280*, 349.
(7) Walsh, D.; Arcelli, L.; Toshiyuki, I.; Tanaka, J.; Mann, S. *Nat. Mater.* **2003**, *2*, 386.
(8) Song, Y.; Yang, Y.; Medforth, C. J.; Pereira, E.; Singh, A. K.; Xu, H.; Jiang, Y.; Brinker, C. J.; van Swol, F.; Shelnutt, J. A. *J. Am. Chem. Soc.* **2004**, *126*, 635.
(9) Biener, J.; Hodge, A. M.; Hamza, A. V.; Hsiung, L. L.; Satcher, J. H. *J. Appl. Phys.* **2005**, *97*, 1.

10.1021/ja056550k CCC: $33.50

Scheme 1. Ammonium Tris(bi(tetrazolato)amine)ferrate(III) Complex (FeBTA)

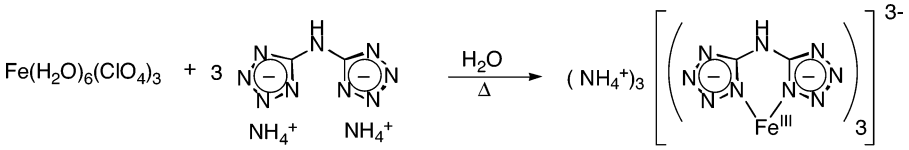

1

templates for use in high-temperature liquid rocket propulsion applications.[10]

In this work we present a relatively simple method to access unprecedented ultralow-density, nanostructured monolithic transition-metal foams, dynamically assembled in a self-propagating combustion synthesis from novel transition-metal complexes containing high nitrogen energetic ligands. During the investigation of the decomposition behavior of the high-nitrogen transition metal complexes, nanostructured metal monolithic foams were formed having remarkably low densities down to 0.011 g cm^{-3} and remarkably high surface areas as high as 270 m^2 g^{-1}. We have demonstrated this technique with the metals iron, cobalt, copper, and silver to form monolithic nanoporous metal foams of varying structures, purities, and structural properties.

Experimental Section

The nanoporous metals produced in this work resulted from the decomposition of metal complexes of the energetic ligand bistetrazolamine (BTA) under inert environments. The first synthesis of BTA ligand was reported by Norris et al.,[11] and later by Highsmith et al.;[12] however, the BTA used to produce the compounds in this study were produced by a method by Naud et al.[13] involving the reaction of a dicyanamide salt with an azide salt, acidified to a pK_a of less than 1. The bi(tetrazolato)amine metal complexes were synthesized in an aqueous solution by reaction of the monohydrated bi(tetrazolato)amine, or ammonium bi(tetrazolo)amine and a metal salt as described elsewhere.[14,15]

Self-propagating combustion synthesis was performed. The complexes were pressed to 6.35 × 6.35 mm^2 pellets at a gauge pressure of 179 kPa to give pellets and of approximately 95% theoretical maximum density and ignited in an environment of N_2 or Ar gas in a 2 L volume combustion chamber by means of a resistively heated nickel−chromium wire.

Scanning electron microscopy (SEM) images were obtained using a LEO 1525. Transmission electron micrographs (TEM) of the nanoporous metal foams were taken on either a FEI Tecnai F30 or Philips CM30 electron microscope operating at 300 kV. Samples were prepared by two methods. In method one, the foam was crushed, and fragments were suspended in alcohol and briefly submerged in an ultrasonic bath for dispersion. A lacey carbon on Formvar 200-mesh copper grid was dipped into the suspension. In method two, pieces of foam were vacuum impregnated with epoxy. The cured sample was then sectioned and dimple polished. A slotted copper support was glued to the sample which was then ion milled.

SEM images at various magnifications were analyzed using Clemex Vision software (Clemex Technologies, Inc.) to determine pore size distribution. All objects in the image were transformed to binary via a gray threshold instruction. This allowed the software to differentiate between the pores and the metal. The software measures the area of each pore. The pore areas were binned in 0.1 μm^2 area increments. The porosity is reported on a volume average and number average basis.

Small Angle Neutron Scattering (SANS) was utilized as a method to determine average sizes of structural features in the foams. The scattered intensity, $I(Q)$, observed in a SANS experiment is directly related to the structure of the sample through the squared Fourier transform of the scattering length density, $\rho(r)$. During a measurement, a fraction of the incident radiation will be scattered into a scattering vector, **Q**, of magnitude $Q = (4\pi/\lambda)\sin\theta$, where λ is the wavelength of the incident neutron and θ is half of the scattering angle, from fluctuations in the scattering length density. $\rho(r)$ then reflects the microscale structure in the sample in both density and chemical and isotopic composition. The complete interpretation of $I(Q)$ in terms of the sample structure, $\rho(r)$, ultimately involves careful comparison with calculations of the scattering expected from model structures. SEM or TEM images are very useful during the initial assessment of SANS data. The real space images provided by SEM and TEM assist in the development of a model for the SANS data, which does not provide a real space image but samples a statistically significant number of particles in a single measurement. SANS data were reduced by conventional methods and corrected for empty cell and background scattering. Absolute intensities were obtained by comparison to a known standard and normalization to sample thickness.

Carbon, hydrogen, and nitrogen (CH&N) measurements were performed on a Perkin-Elmer 2400 Series II CHNS/O Analyzer, BET surface areas were measured on a QuantaChrome Autosorb-1, and TGA measurements were performed using a TA Instruments Hi-Res Modulated TGA 2950 Thermogravimetric Analyzer.

Results and Discussion

Iron Foams. The nanoporous metal foam monoliths produced in this work arose from the decomposition of metal complexes of the energetic ligand bistetrazolamine. Ignition of ammonium tris(bi(tetrazolato)amine)ferrate(III) complex (Fe-BTA) (Scheme 1) as a loose powder in air results in a vigorous burn, with the production of orange sparks indicative of the burning of nascent iron in air. However, the combustion of cylindrical pellets of Fe-BTA in a combustion chamber of nitrogen atmosphere at varying pressures results in the formation of the metal foam monolith (Figure 1). Evidently, the high-nitrogen ligand acted as a blowing agent on a molecular level as Fe-BTA decomposed, liberating decomposition gases, while the metal centers were reduced to an oxidation state of zero, and dynamically assembled into porous monoliths. The synthesis results in a dramatic increase in length (roughly 5 times) from the compressed Fe-BTA pellet to the metal foam, with very little change in the diameter from pellet to foam. This effect can be explained due to the nature of the dynamic assembly of solid products after the passage of the planar flame front in the material, with the bulk of the gases and coalescing metal being directed away from the pellet surface.

The combustion synthesis is a dynamic and complex process. Evidently, the high-nitrogen ligand provides both a blowing

(10) Sherman, A. J.; Williams, B. E.; Delarosa, M. J.; Laferla, R. In *Mechanical Properties of Porous and Cellular Materials*; Sieradzki, K., Green, D., Gibson, L. J., Eds.; Materials Research Society Symposium Proceedings 207; Materials Research Society: Pittsburgh, PA, 1991; p 141.
(11) Norris, W. P.; Henry, R. A. *J. Org. Chem.* **1964**, *29*, 650.
(12) Highsmith, T. K.; Hajik, R. M.; Wardle, R. B.; Lund, G. K.; Blau, R. J. U.S. Patent 5,468,866, 1995.
(13) Naud, D. L.; Hiskey, M. A. U.S. Patent 6,570,022, 2003.
(14) Chavez, D. E.; Hiskey, M. A.; Naud, D. L. *J. Pyrotech.* **1999**, *10*, 17.
(15) Tappan, B. C.; Huynh, M. H.; Hiskey, M. A.; Chavez, D. E.; Son, S. F.; Oschwald, D. M. U.S. Patent (submitted).

Figure 1. Photograph of iron foam next to unburned pellet of the Fe−BTA complex.

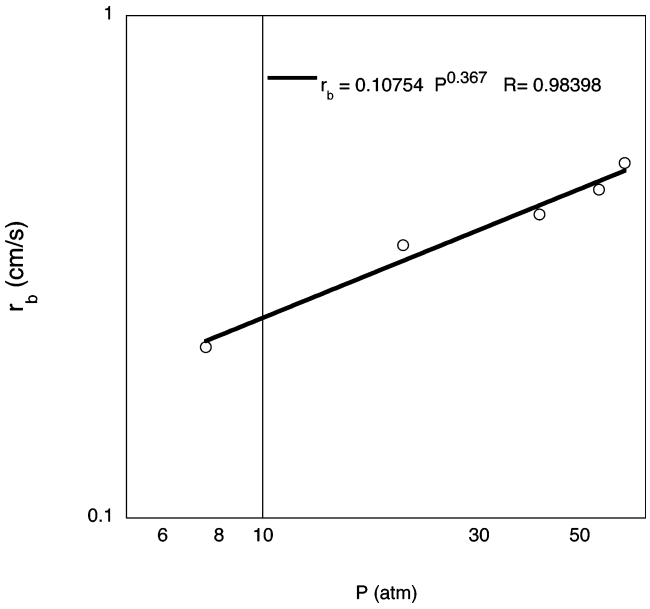

Figure 2. Burning rate of Fe−BTA vs Ar pressure showing the slow burning rate of 0.51 cm s^{-1}, atypical of metal containing energetic materials and small burning rate exponent of 0.367.

agent and heat, on a molecular level as Fe−BTA decomposes, liberating decomposition gases. It is clear that as the metal complex is burned, metal centers are liberated from the BTA complex and must rapidly find binding sites to satisfy bonding requirements. It is remarkable that the metal centers are capable of finding binding sites while large amounts of gas are evolved. Still more unpredictable is the result that a nanoporous, three-dimensional network is produced instead of a disperse powder.

This method is made possible because of the unique burning characteristics of these materials. Compared to other energetic metal-containing compounds, these complexes are fairly unique in that they exhibit steady burning behavior, rather than very rapid burning or even detonation typical of this class of compounds. Figure 2 shows the burning rate of the Fe-BTA vs pressure, and we observe that even at the highest pressure (burning rate of energetic materials increases exponentially with pressure) the rate of burning is only 0.51 cm s^{-1}. In contrast,

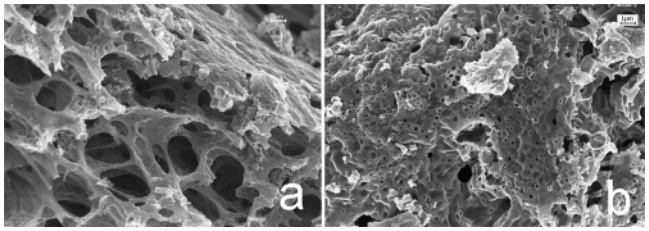

Figure 3. (a) Scanning electron micrograph (SEM), 1 μm scale, of low pressure iron foam showing a pore structure of roughly 1 μm. (b) SEM, 1 μm scale, of high pressure iron foam showing a pore substructure of roughly 20−100 nm.

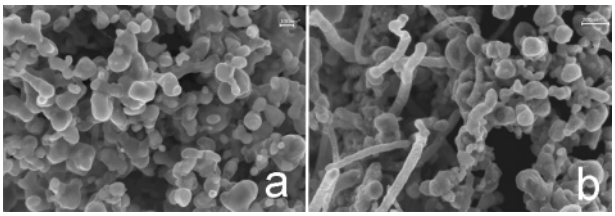

Figure 4. (a) SEM, scale 100 nm, of Fe foam after heat treatment to 800 °C Ar. (b) SEM, scale 200 nm, of Co foam after heat treatment to 800 °C Ar; foam walls were made up of particles, and rods, of cobalt metal.

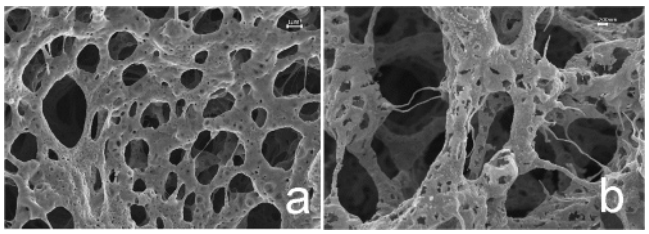

Figure 5. (a) SEM image, 1 μm scale, of Fe foam prior to heat treatment, and (b) SEM image, 200 nm scale, of Fe foam from (a) showing no sintering after 500 °C heat treatment under H_2 flow.

most energetic metal compounds transit from burning to detonation in very small diameters; for example the common primary explosive silver azide (AgN_3) detonates at a velocity of 5.9 km s^{-1}, with no observable burning phase prior to detonation.[16] Certainly any zerovalent metal formed in this process will be very fine particles and very widely scattered.

Furthermore, the presence of hydrogen due to the ammonia ligand or ammonium counterions provides a reducing environment directly at the flame front, allowing the nascent metal atoms to quickly convert to the zerovalent state. Following combustion at 2.07 MPa (20 atm) of nitrogen, a polymodal pore size distribution was observed, dominated by a small number fraction yet large volume fraction of pores in the 1−3 μm range, and then within the ligaments of foam, pores in 20−200 nm range dominate the number fraction distribution (Figure 3a). Interestingly, combustion at 7.33 MPa (69 atm) resulted in a metallic foam containing almost entirely the 20−200 nm pore size distribution as determined by analysis of SEM images (Figure 3b). BET surface area analysis for the metal foam produced at 2.07 MPa (20 atm) yielded an extraordinarily high surface area of 258 m^2 g^{-1} and density of 0.011 g cm^{-3}. BET surface area for foams produced at higher pressures (7.3 MPa, 69 atm) ranges from 12 to 17 m^2 g^{-1} and a density of 0.040 g cm^{-3}.

A number average pore size analysis revealed that there are 2 orders of magnitude more small pores (0.1 μm^2) than large

(16) Persson, P. A.; Holmberg, R.; Lee, J. *Rock Blasting and Explosives Engineering*; CRC Press: Boca Raton, FL, 1994.

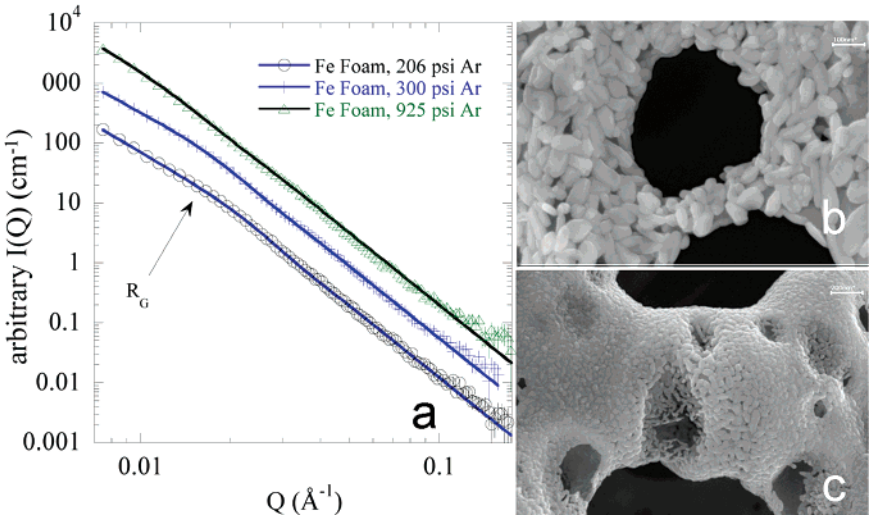

Figure 6. (a) SANS data for Fe foams showing a decrease in average structural size with lower pressure, as seen in Table 1. (b) SEM, 100 nm scale, Fe foam showing grain sizes of roughly 30−50 nm. (c) SEM, 200 nm scale, of Fe foam formed at a lower pressure than that of (b) showing qualitatively smaller grain sizes of 10−50 nm.

pores (1 μm^2) with the largest pores (>10 μm^2) being very infrequent. Interestingly, this distribution is the same for both the as-synthesized and heat-treated foams despite the visual changes and change in surface area. The total area of the largest pores is about one-quarter of the total area of the smallest pores; consequently the largest pores contribute significantly to the measured density of the iron foams. The largest pores are also expected to dominate the mechanical properties of the foams.

Energy dispersive spectra (EDS) demonstrate that the as-produced iron foams contain residual carbon and nitrogen in addition to Fe metal. Elemental analysis (standard combustion technique) confirmed that the Fe foam was approximately 50% metal, with the remainder being varying amounts of C and N. Following formation of the metallic monoliths, heat treatment under a flow of Ar or H_2 gas was performed on the Fe foams. By thermogravimetric analysis (TGA) it was determined that a temperature of 800 °C (1073 K) was sufficient for the most complete evaporation of unspecified carbon and nitrogen impurities from the metal foam under an inert flow of Ar, and a temperature of 500 °C (773 K) under a reducing H_2 flow was sufficient to reduce residual impurities from the metal foam. Thermogravimetric analysis (TGA) and EDS indicate that the heat-treated Fe foams at 800 °C under Ar contain 10% carbon. While no density or surface area measurements were made on the Ar heat-treated foam due to small sample size, it is apparent from the SEM images of both Fe and Co discussed below that while there was a change in the morphology, no significant sintering took place (Figure 4a and b). After the Fe foam was heat-treated under a H_2 gas flow to 500 °C, a dramatic increase in surface area was observed. The surface area of this material increased from a value of 20 g^{-1} before heat treatment to a value of 120 m^2 g^{-1} after heat treatment, further confirming the observation that this material is not sintering, as seen in the SEM images in Figure 5a and b. There are two reasons for this: first, the removal of significant mass of the volatile/reducible elements competes with the densification, and second, sintering is constrained by stresses in the foam structure during the short duration of heating.[17] The average grain size of the iron foam was estimated from SEM and TEM images to be about 25 nm. There was no significant increase in grain size after heat treatment.

Table 1. Average Sizes of Structural Component Determined by SANS of Fe Foam vs Pressure under Which It Was Formed

P (psi)	R_{sphere} (Å)
206	146 ± 1
300	182 ± 1
925	232 ± 6

Figure 6 shows the SANS line shapes measured for Fe foams at three different pressures. The log−log plot of the scattered intensity shows three distinct features. At the lowest *Q*-values measured ($Q < 0.01$ Å^{-1}), the data falls off as a simple power law ($I(Q) \propto Q^{-\alpha}$). This is followed by a Guinier region (as indicated by the arrow in the figure) and then a second power law region. This type of SANS line shape is indicative of multiple length scales within the foam, and we have thus used the *unified model* of Beaucage to interpret the data.[17]

The solid lines in the figure are the result of analysis by the *unified model*. From the analysis, we found that the data from all of the Fe foams displays a noninteger power law with an exponent of 2.9 ± 0.2 in the low-*Q* region of the data. Within the error of the measurement, this indicates a surface fractal arrangement of scatterers. The Guinier region, which indicates the average size of the scatterer, was found to shift to lower *Q*-values with increasing pressure, suggesting an increase in the average size of the scatterer. At these lengthscales (50−1 nm), the measured intensity is most likely arising from the struts which make up the foam. From the SEM image (Figure 6b and c), we see that the struts consist of an arrangement of polydisperse Fe particles, which are also seen in the Co foams, discussed in further detail in the following section. The scattering then arises from these particles or the free volume (pores) within the struts. Assuming that the scattering bodies are spherical in shape, their average sizes were determined and are listed in Table 1. In the high-*Q* region, all curves fall off with an exponent, $\alpha = 4$, indicating smooth, nonfractal interfaces at the smallest lengthscales.

(17) Beaucage, G. *J. Appl. Crystallogr.* **1995**, *28*, 717.
(18) Evans, A. G.; Hsueh, C. H. *J. Am. Ceram. Soc.* **1986**, *69*, 444.

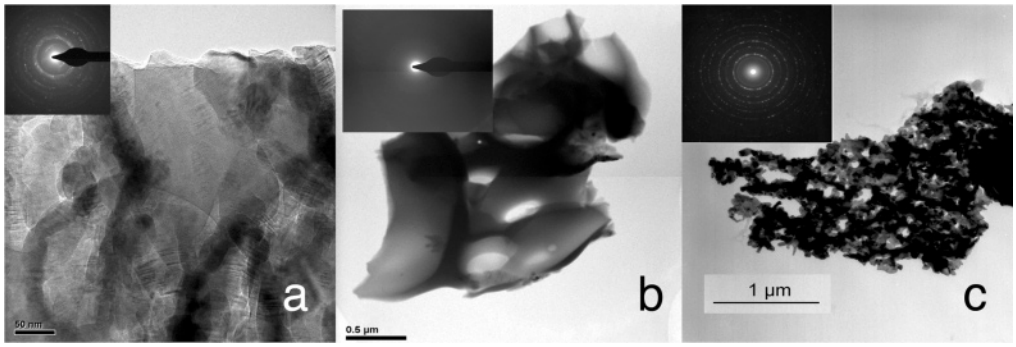

Figure 7. (a) TEM of crystalline region of Fe foam with selected area diffraction pattern, scale 0.2 μm. (b) TEM of amorphous region of Fe foam with selected area diffraction pattern, scale 0.5 μm. (c) TEM of Fe foam after heat treatment with selected area diffraction pattern, scale 1 μm.

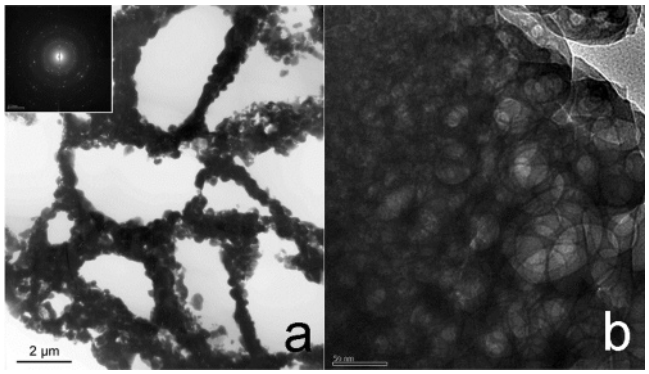

Figure 8. (a) TEM of Cu with selected area diffraction pattern, scale 2 μm. (b) TEM image of Cu showing extensive close pore structure, scale 50 nm.

TEM images of iron foams before and after heat treatment are seen in Figure 7a−c (note the difference in magnification). Although, the average particle size is not greatly changed, the crystallite and pore morphologies are strongly affected by the heat treatment at 500 °C. This is a consequence of the removal of volatile elements (carbon, nitrogen, and oxygen) and crystallization of the iron. Selected area diffraction indicates a phase change from somewhat ambiguous patterns tentatively index matched to hexagonal Fe_3N and orthorhombic iron carbide to a clearly defined alpha-iron (body centered cubic). It was also qualitatively observed that the Fe foam was not perceptibly magnetic prior to heat treatment but was strongly magnetic afterwards. Although Fe_3N and iron carbide are magnetic phases, since they are nanocrystalline with a high surface area, there is a high volume of interfaces which tend to be weakly magnetic. Figure 7b shows a TEM image of an amorphous region of the Fe foam. EDS analysis indicated that this region is predominantly carbon but also contains nitrogen and iron. Although amorphous regions were not common, several were observed in the as-synthesized samples.

Cu, Co, and Ag Foams. The reduction of the transition metal through combustion in these complexes appears to be general, with possibly many more transition metals utilized. Cobalt, silver, and copper metal foams have been produced from the corresponding analogues of, or similar compounds to, Fe-BTA. The morphology of the resultant foam is strongly dependent on the transition metal employed. The copper foam prior to heat treatment was of a higher density ($\sim$0.9 g cm^{-1}) and much stronger than the iron foam and had much more regular yet larger open-pore sizes of approximately 1−2 μm (Figures 8a and 9b), with considerable close pore structure throughout the foam walls on the order of 20−50 nm. Weight loss in TGA and CH&N analysis indicate that the Cu foam, prior to heat treatment, typically contains about 70% Cu metal. After heat treatment, EDS indicates that the Cu foam is essentially the pure metal.

TEM images of copper foams before and after heat treatment are seen in Figure 8. Similar to the iron foam, the heat treatment results in morphological changes that are explained by the removal of the lighter elements and crystallization of copper. In the case of the copper, the structural change was more profound. Heat treatment to 800 °C in Ar appears to significantly coarsen the pores, and the copper crystals take on a highly faceted habit. Although small pores remain, they tend to resemble cracks due to the facets of the crystals bounding the pore. Heat treatment to 500 °C in H_2 resulted in a foam with many small, highly faceted crystallites that appear to be forming out of the foam walls, Figure 9b. In contrast to the iron foams, selected area diffraction patterns of the as-synthesized copper foams show crystalline carbon. After heat treatment, crystalline copper (face centered cubic) was readily observed. No amorphous regions were observed.

Figure 9a displays SANS data from a Cu foam before and after heating. The data are similar in nature to the Fe foams in that they display the same initial power law falloff ($\alpha = 2.9 \pm 0.2$), followed by a Guinier region and a second power law region with $\alpha = 4$. For the Cu foams, the Guinier region appears at larger Q-values, indicating a smaller average size of the particles or pores within the struts. We see from these data that, assuming spherical shapes for the scatterers, their average size decreases by $\sim$20% after heat treatment, with the R_{sphere} for the as-formed Cu foam being 78 $\pm$ 4 Å and after heat treatment being 62 $\pm$ 3 Å.

Electron micrographs of the cobalt foam showed not only the two basic pore morphologies observed in the Fe foam but also a third morphology consisting of small Co grains ($\sim$10 nm) that aggregate to form the foam walls (Figure 10a). This feature, while observed in the Fe foam, was much more prominent in the Co foam.

The silver foam was the densest material made and, in fact, had fused together in portions to form shiny silver beads, with limited regions of foam similar to the other metals utilized. This is due to a high molecular content of Ag in the complex compared to the other complexes, with only one BTA ligand for every two Ag atoms. In the porous areas of the silver metal, the larger pore sizes are in the range of 1 μm, and the smaller, nonconnected surface porosity is approximately 20 nm in size,

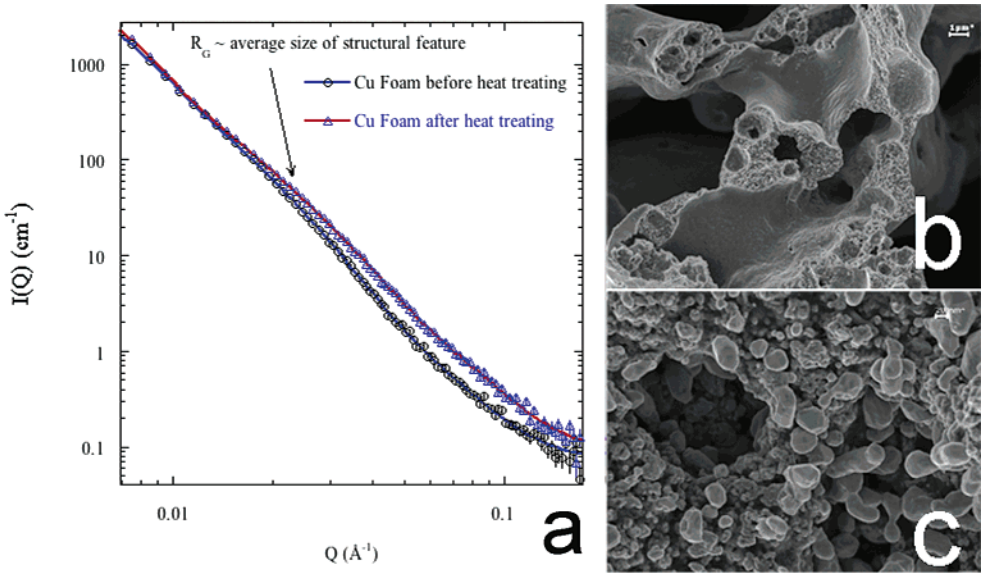

Figure 9. (a) SANS for Cu showing the average size decreases of structural features in walls by ~20% after heat treatment, with the R_{sphere} for the as-formed Cu foam being 78 ± 4 Å and after heat treatment being 62 ± 3 Å. SEM, 200 nm scale, of heat-treated copper foam 800 °C Ar. (b) SEM, 1 μm scale, of as-formed Cu foam as measured in (a). (c) SEM, 200 nm scale, of heat-treated copper foam at 500 °C H_2 as measured in (a).

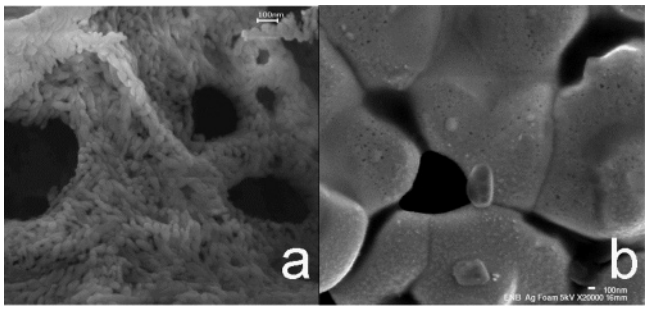

Figure 10. (a) SEM, 100 nm scale, Co foam showing grain sizes of roughly 10−50 nm. (b) SEM, scale 100 nm, of porous area of Ag foam showing surface nanoporosity of around 20 nm.

as seen in Figure 10b. This foam portion indicates that when an optimized formulation of the silver complex and gas generate (such as additional BTA precursor) is produced, monoliths comparable to the Cu, Fe, or Co foams can likely be achieved.

Structural differences in the as-synthesized materials may be due not only to the differences in metal−BTA complex structure, ligand content, and melting points of the metals but also to the relative solubility of volatile elements (carbon and nitrogen) in the matrix. For example, crystalline carbon was observed in as-synthesized copper foams, whereas amorphous carbon was seen in the as-synthesized iron foams. It is possible that carbon crystallization occurs in the copper foams due to an anticipated higher carbon purity as a consequence of the low tolerance of copper for carbon.

Summary

This new technique shows promise for being a flexible, general approach to the formation of a wide range of new nanoporous metals not currently accessible by state-of-the-art nanoscience. We have demonstrated the ability to form foams of metals with differing chemistries and crystal structures including iron (BCC), cobalt, copper (FCC), and silver. The structural characteristics (surface area, pore size, density, etc.) of the metal foams vary with composition and as a function of precursor chemistry (number of ligands) and overpressure during combustion. Removal of volatile elements (carbon and nitrogen) is possible by heat treatment at modest temperatures in inert or reducing atmospheres. The heat treatment does not collapse (sinter) the foam and, due to mass removal and constrained sintering, can increase the surface area. Heat treatment has the added benefits of mechanically strengthening the foam and promoting crystallization and phase changes. In the case of iron, heat treatment induces a phase change from nonmagnetic phases appearing to be orthorhombic iron carbide and hexagonal Fe_3N to a clearly defined magnetic alpha-iron (body centered cubic) phase. Some differences in the structure of the as-synthesized materials may be due to the relative solubility of volatile elements (carbon and nitrogen) in the matrix.

Further work is underway to optimize the Ag foam and expand the variety of metals produced. Possible applications for this new class of materials abound in the fields of catalysis, fuel cells, hydrogen storage, unique insulation, and electromagnetic absorption materials to name but a few.

Acknowledgment. This work was funded under B.C.T.'s Agnew National Security Postdoctoral Fellowship in addition to the joint DoD/D.O.E. Munitions Technology Development Program. We thank David M. Oschwald, Ed L. Roemer, and Eric N. Brown for the SEM images and Bettina L. Smith, Lloyd L. Davis and Jose G. Archuleta, and Anna M. Giambra for BET, CH&N, and TGA. Thanks to Thomas Lienert and Rob Dickerson of Los Alamos National Laboratory for helpful conversations and TEM assistance. Many thanks as well to Juergen Biener, Sergei Kucheyev, and Morris Wang of Lawrence Livermore National Laboratory for many helpful conversations and an additional TEM image. Los Alamos National Laboratory is operated by the University of California for the D.O.E. under Contract W-7405-ENG-36.

Supporting Information Available: A short video of the formation of iron foam in Figure 1 is available. This material is available free of charge via the Internet at http://pubs.acs.org.

JA056550K